EES Batteries

PAPER

View Article Online
View Journal | View Issue

Cite this: *EES Batteries*, 2025, **1**, 1665

Seamlessly connected cathode–gel electrolyte interfaces enable highly stable aqueous zinc batteries

Yuguo Zheng,†[a] Liting Gao,†[b] Xin Liu,†[a] Yige Wang,[a] Jiahao Li,[a] Jiachen Li,[b] Zhansheng Guo,*[b] Yizhou Zhang*[c] and Hanfeng Liang*[a]

Received 30th July 2025,
Accepted 27th September 2025

DOI: 10.1039/d5eb00143a

rsc.li/EESBatteries

Gel electrolytes are widely adopted in aqueous Zn batteries to mitigate water-induced side reactions and cathode dissolution. However, conventional designs with physically isolated cathodes and gel electrolytes create high-resistance solid–quasi-solid interfaces that limit performance. Here, we propose a seamlessly connected cathode–gel electrolyte interface design by constructing an integrated cathode–gel electrolyte configuration, which is achieved by *in situ* generation of a polymer network within the cathode and its further crosslinking with the polymer matrix of the *in situ* grown gel electrolyte. As a result, the cathode active material is tightly encapsulated by the polymer network and the outwardly growing gel electrolyte, which not only effectively shortens the ionic transport pathway and enhances the diffusion kinetics, but also suppresses the dissolution of the cathode active material. Consequently, the assembled Zn||$Mg_{0.1}V_2O_5$ batteries with this novel design possess significantly improved performance with a high capacity of 200 mAh g^{-1} at 0.5 A g^{-1} after 900 cycles. However, the battery with a conventional design suffers from capacity decay and battery failure within 600 cycles under the same conditions. This work provides a general strategy to greatly enhance the electrochemical performance of Zn batteries by constructing seamlessly connected electrode–electrolyte interfaces and might be applied to many other aqueous battery systems.

Broader context

This study introduces a novel seamlessly connected cathode–gel electrolyte interface design, which addresses critical challenges in aqueous Zn batteries, such as high-resistance interfaces and cathode dissolution. The proposed strategy integrates the cathode and gel electrolyte into a unified structure through *in situ* polymer network generation and crosslinking, leading to improved ionic transport and enhanced cathode stability. This design results in significantly improved battery performance, demonstrating a high capacity of 200 mAh g^{-1} after 900 cycles, compared to the rapid capacity decay and failure observed in conventional designs. The impact of this advancement on energy and environmental science is substantial. By enhancing the efficiency and lifespan of aqueous Zn batteries, this work paves the way for more sustainable and reliable energy storage systems. Furthermore, the unique integrated electrode–electrolyte design holds promise for other aqueous battery systems, offering a versatile solution for addressing the limitations of current energy storage technologies.

Introduction

With the large-scale promotion and application of renewable energy sources such as wind, solar, and geothermal energy, the demand for safe and cost-effective energy storage systems is rapidly increasing. Traditional lithium-ion batteries are limited by cost and safety concerns, while aqueous zinc batteries present a promising alternative.[1–3] Zinc batteries utilize aqueous solutions as electrolytes, which reduces the overall cost and ensures high ionic conductivity.[4] However, the aqueous electrolytes also induce side reactions and promote the dissolution of cathode materials such as Mn and V oxides, leading to unsatisfactory cycling performance.[5]

[a]*State Key Laboratory of Physical Chemistry of Solid Surfaces, College of Chemistry and Chemical Engineering, Xiamen University, Xiamen 361005, China. E-mail: hfliang@xmu.edu.cn*
[b]*Shanghai Institute of Applied Mathematics and Mechanics, School of Mechanics and Engineering Science, Shanghai Key Laboratory of Mechanics in Energy Engineering, Shanghai University, Shanghai 200072, China*
[c]*Institute of Advanced Materials and Flexible Electronics (IAMFE), School of Chemistry and Materials Science, Nanjing University of Information Science & Technology, Nanjing 210044, China*
† These authors contributed equally to this work.

To enhance the cycling stability of aqueous zinc batteries, hydrogel electrolytes are often employed as substitutes for traditional aqueous electrolytes.[6] Hydrogel electrolytes are a class of gel polymer electrolytes that are made of crosslinked hydrophilic polymer networks that can absorb and retain a significant amount of water.[7] These polymers can either be synthetic polymers like polyacrylamide (PAM),[8] polyacrylic acid (PAA),[9] and polyvinyl alcohol (PVA),[10] or natural polymers such as cellulose,[11] sodium alginate,[12] and gelatin.[13] Composite gel electrolytes, such as PAM/PVA[14] and PAM/PPR,[15] have also been extensively studied. The backbone polymers have abundant functional groups, such as carboxyl and hydroxyl groups, which could regulate the solvation structure of Zn^{2+} ions by forming hydrogen bonds with water molecules. This reduces free water content and minimizes side reactions, leading to a prolonged cycling lifespan.[16]

However, in a conventional battery configuration, the cathode and gel electrolyte are isolated, resulting in a distinct solid–quasi-solid interface and consequently large interfacial resistance (Scheme 1a), in contrast to the relatively smooth solid–liquid interface in aqueous electrolyte systems.[17] The H_2O, Zn^{2+}, and H^+ ions in gel electrolytes must traverse through the poorly connected solid interface and diffuse to the cathode. This creates long diffusion pathways and consequently leads to slow kinetics, hindering ion transport.[18] Therefore, an "activation process" is often observed in batteries with gel electrolytes. Additionally, the continuous intercalation and deintercalation of Zn^{2+} and H^+ ions at the cathode lead to the irreversible dissolution of the active material.[19] Herein, we address these key issues by constructing seamlessly connected cathode–gel electrolyte interfaces through *in situ* generation of gel electrolytes that encapsulate the active cathode material. Specifically, the electrolyte precursor solution penetrates deeply into the cathode, where it undergoes polymerization to form a hydrogel electrolyte under UV irradiation, creating an integrated cathode–gel electrolyte configuration (Scheme 1b). Simultaneously, the organic acrylic acid (AA) monomers within the cathode polymerize to form a PAA network, which further chemically crosslinks with the hydrogel electrolyte's polymer backbone, resulting in a robust integrated structure. This design mimics the properties of liquid electrolyte systems, which shortens the ion conduction pathway and facilitates ion transport.

Using a vanadium-based cathode material, $Mg_{0.1}V_2O_5$ (MVO), as an example, we showed both experimentally and theoretically that such an integrated design can effectively enhance the ionic diffusion and suppress the dissolution of the active material. Consequently, the cycling stability of the assembled Zn-MVO batteries is significantly improved with a high capacity of 200 mAh g^{-1} after 900 cycles at 0.5 A g^{-1}. However, the conventional design suffers from battery failure within 600 cycles under the same conditions. The effectiveness and versatility of the integrated cathode–gel electrolyte configuration are further verified in Zn||MnO_2 batteries.

Results and discussion

The integrated cathode–gel electrolyte structure was achieved by a photo-induced crosslinking method (see details in the Method section, SI). Specifically, we introduced acrylic acid (AA) into the cathode slurry and then drop-cast the hydrogel electrolyte precursor solution onto the cathode to allow efficient penetration of the electrolyte. UV irradiation was then applied to induce the conversion of the hydrogel precursor into a gel electrolyte evenly distributed within the cathode. Meanwhile, the AA monomers in the cathode underwent crosslinking polymerization into a robust polyacrylic acid (PAA) network, which further crosslinks with the polymer matrix of an *in situ* grown gel electrolyte. This not only immobilizes the cathode active material but also creates a cathode–electrolyte integrated structure with seamlessly connected interfaces (referred to as integrated cathode thereafter, Fig. S1 and S2). For comparison, we also fabricated a crosslinked cathode (by UV irradiation of MVO with AA additives) and a pristine cathode (*i.e.*, MVO with AA additives) (Fig. 1a–c).

We then conducted X-ray diffraction analysis and the result reveals that the addition of AA and further UV irradiation do not alter the structure of the MVO (Fig. 1d and S3). However, Fourier transform infrared spectroscopy (FT-IR) indicates subtle differences between these cathodes. Specifically, the FTIR spectrum of the pristine MVO cathode with the AA addi-

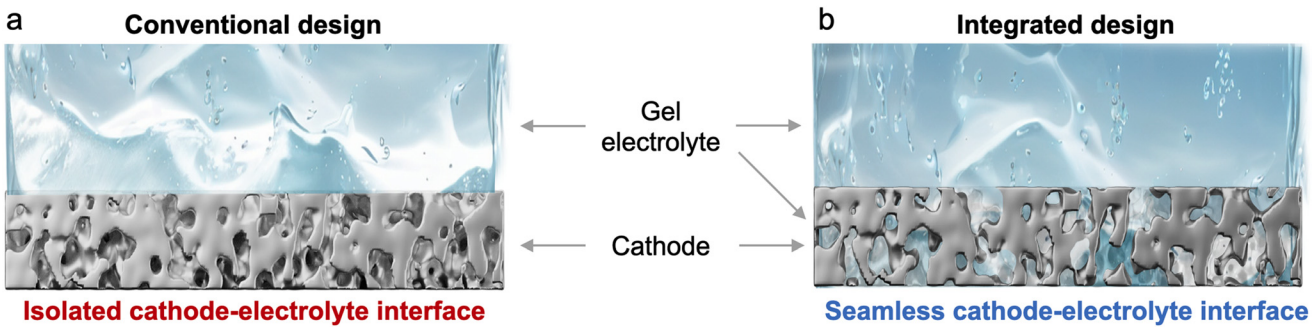

Scheme 1 Schematic illustrations of (a) the isolated cathode–electrolyte interface and (b) the seamless cathode–electrolyte interface.

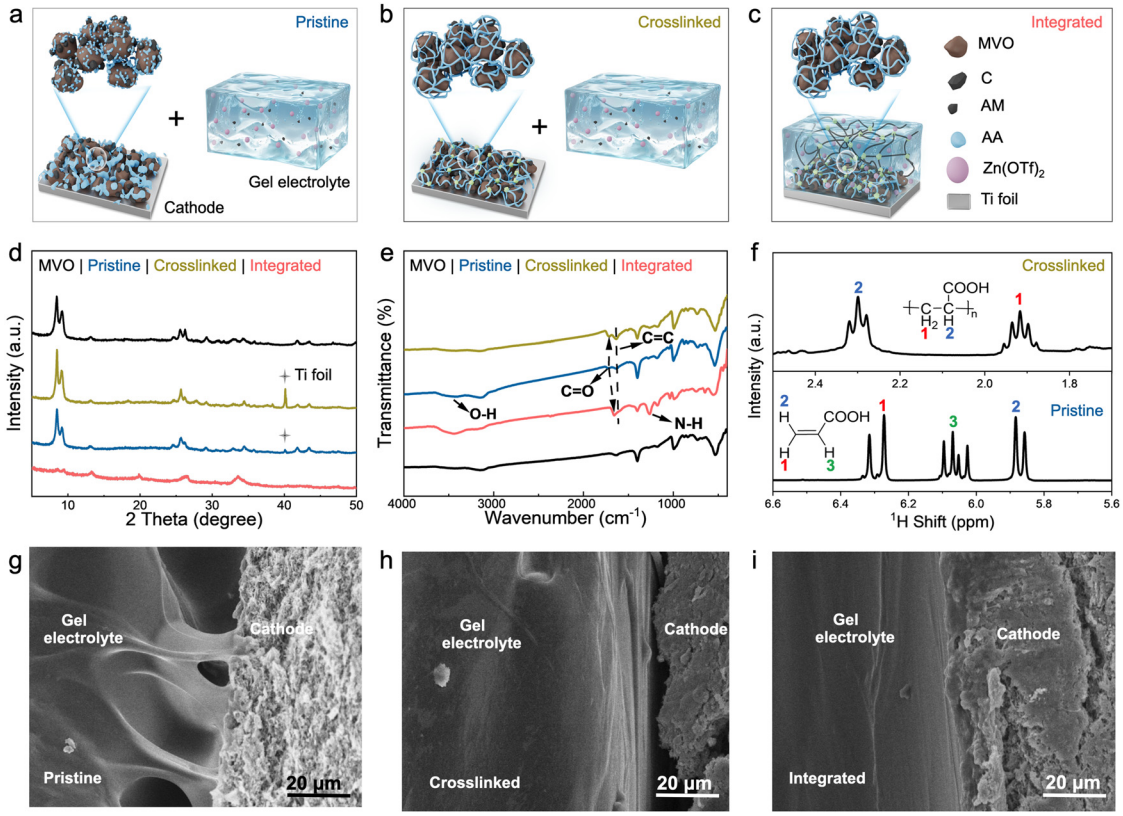

Fig. 1 Characterization of *in situ* photopolymerization and the integrated cathode–gel electrolyte structure. The compositional schematic of (a) pristine, (b) crosslinked, and (c) integrated cathodes. (d) XRD patterns of MVO, pristine, crosslinked, and integrated cathodes. (e) FT-IR spectrum of MVO, pristine, crosslinked, and integrated cathodes. (f) ^{1}H NMR of pristine and crosslinked cathodes. Cross-sectional SEM images of the interface between hydrogel electrolytes and (g) pristine, (h) crosslinked, and (i) integrated cathodes.

tive exhibits stretching vibration peaks of C=O at 1725 cm^{-1} and O–H at 3300–3500 cm^{-1}, respectively. Meanwhile, for the crosslinked cathode, the C=O peak shifts to lower wavenumbers. For the integrated cathode, the C=O characteristic peak also shows a blue shift compared to that of the pristine cathode. Additionally, the peak of C=C at 1630 cm^{-1} disappears, and the peak at 1268 cm^{-1} corresponding to –NH stretching vibration appears. This result confirms the presence of AM and further its polymerization with AA (Fig. 1e).[20–22] We also conducted ^{1}H nuclear magnetic resonance spectroscopy (NMR) analysis of the pristine and crosslinked cathodes (we failed to conduct the analysis of the integrated cathode due to the difficulty in separating the gel electrolyte and the cathode material). The NMR spectrum of the pristine cathode reveals three quadruplets at 5.95, 6.05, and 6.3 ppm, respectively, corresponding to different types of H in AA, in agreement with previous reports (Fig. 1f),[23] while for the crosslinked cathode, the characteristic peaks of methylene and methyl groups appear at 1.9 and 2.3 ppm, respectively.[24] This confirms the successful introduction of AA into MVO and its polymerization into PAA after UV irradiation. Indeed, the scanning electron microscopy (SEM) images show that the pristine cathode consists of randomly distributed MVO nanorods, whereas the surface of the crosslinked cathode is covered by large pieces of PAA polymers (Fig. S4), which increases the water contact angle from 37° for the pristine cathode to 58° for the crosslinked cathode (Fig. S5).

A closer SEM observation reveals a significant gap between the cathode and the gel electrolyte for both the pristine and crosslinked cathodes (Fig. 1g and h), which would lead to an increased interfacial resistance and thus reduce the diffusion kinetics. For the crosslinked cathode, the large pieces of hydrophobic PAA layers on the surface introduce additional resistance and could further reduce the reaction kinetics. In contrast, the integrated cathode displays a seamlessly connected interface (Fig. 1i). In addition, the elemental mapping of the cross-section reveals the uniform distribution of Zn and S elements, indicating deep permeation of the gel electrolyte into the MVO cathode (Fig. S6). This highly integrated cathode–gel electrolyte configuration is expected to promote the ionic diffusion and further enhance the interaction between the cathode and the electrolyte, leading to boosted electrochemical performance.

For all three cathodes, the CV curves possess two couples of redox peaks, corresponding to the successive Zn^{2+} insertion and desertion (Fig. 2a and S8–S10). Compared to the pristine cathode, the redox peak intensity of the crosslinked cathode is greatly reduced, suggesting a suppressed activity of the MVO.

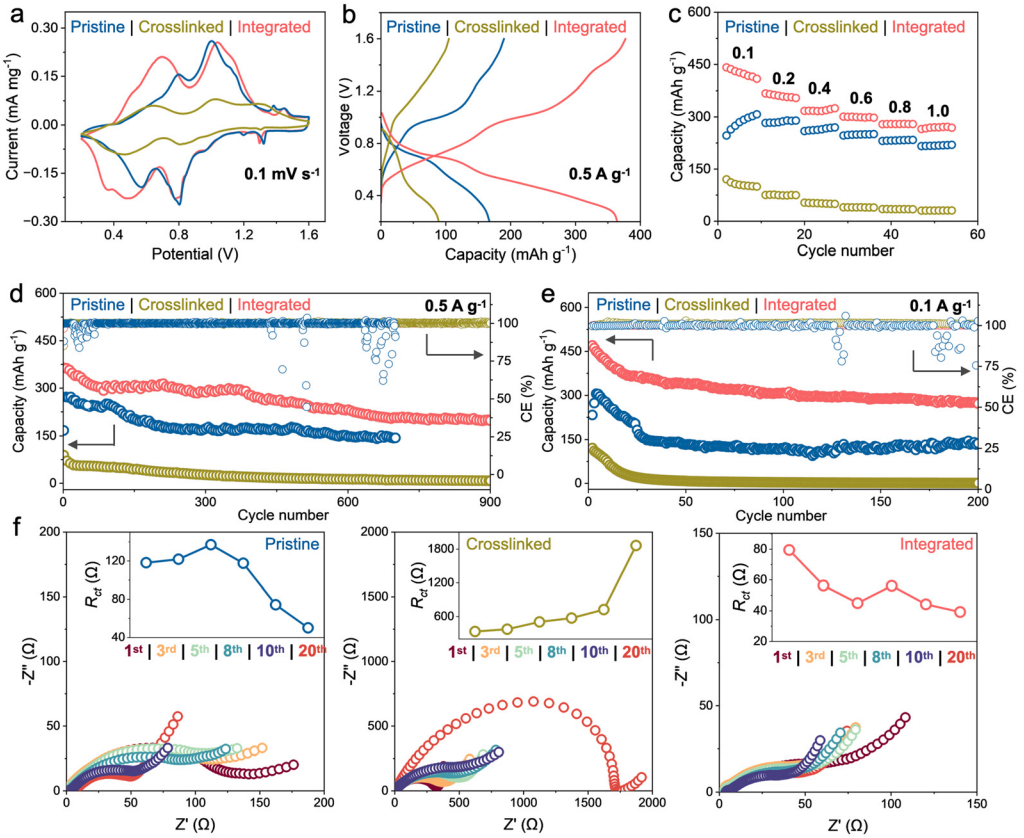

Fig. 2 Cathode–electrolyte integration achieves better electrochemical performance. (a) CV profiles, (b) charge–discharge curves, and (c) rate performance evaluation of the full batteries. (d) Cycling performance at 0.5 A g^{-1}. (e) Cycling performance at 0.1 A g^{-1}. (f) Impedance spectra of full batteries from the 1st to 20th cycles.

This is due to the surface PAA network that blocks the active MVO as well as the increased hydrophobicity. However, for the integrated cathode, the first couple of redox peaks shift to lower potentials, indicating that Zn^{2+} insertion and desertion would proceed easier thanks to the seamlessly connected interfaces.[25] Moreover, it also exhibits the largest peak area, pointing to an enhanced capacity. Indeed, the integrated cathode delivers a high capacity of 364.2 mAh g^{-1} at 0.1 A g^{-1}, much higher than that of the pristine and crosslinked cathodes (167.2 and 89.1 mAh g^{-1}), respectively (Fig. 2b). We further evaluated the rate performance of the three cathodes. The integrated cathode again exhibits the highest capacities at various current densities (Fig. 2c and S11). Besides the superior rate capability, the integrated cathode also exhibits high cycling stability with a high reversible capacity of 200 mAh g^{-1} even after 900 cycles at 0.5 A g^{-1} (Fig. 2d and S12). In contrast, the pristine cathode suffers from capacity decay and further battery failure within 600 cycles. It is noted that the crosslinked cathode shows much worse performance, with the capacity quickly dropping to 27 mAh g^{-1} within 300 cycles, due to the presence of a large amount of PAA on the MVO surface. The above results clearly demonstrate that batteries with a seamless design exhibit superior performance compared to those with a conventional design. More importantly, even at a low N/P ratio of 1.34 (currently 6.7), the integrated cathode still delivers high capacity and stability at 0.5 A g^{-1} (Fig. S13). It is also worth mentioning that here we used a low concentration of Zn salt, *i.e.*, 1 M $Zn(OTf)_2$, whereas higher concentrations (*e.g.*, 2 M or 3 M) are known to greatly enhance the performance and are more commonly used in the literature (they also come with increased costs). In fact, the performance of the integrated cathode in our work can be also greatly enhanced if a higher concentration (*e.g.*, 3 M) of zinc salt is used. The capacity is more than 600 mAh g^{-1} and a high stability is maintained (Fig. S14).

We also observed an interesting phenomenon: the integrated cathode quickly reaches the full capacity, whereas the pristine cathode experiences a gradual capacity increase in the initial cycles, which is typically referred to as the so-called "activation process" (will be discussed later). Subsequent cycling performance tests were conducted at lower current densities (*e.g.*, 0.1 A g^{-1}), which typically necessitate a longer "activation process" because of the lower energy. However, a similar trend is still observed. The integrated cathode does not undergo the "activation process" but reaches the full capacity at the very beginning (Fig. 2e), indicating significantly promoted reaction kinetics as well as largely enhanced cathode–electrolyte interactions thanks to the seamlessly connected

cathode–electrolyte interfaces. Electrochemical impedance was measured in different cycles (Fig. 2f). During cycling, the charge transfer impedance of the pristine cathode increases and then decreases due to the "activation process", while that of the crosslinked cathode experiences a significant and continuous increase due to the presence of the surface coated PAA polymer network. In contrast, the impedance of the integrated cathode shows a gradually decreasing trend. This difference can be attributed to the integrated structure of the PAA polymer and hydrogel matrix in the integrated cathode, which enhances the diffusion kinetics of H_2O and cations. It should be noted that the polymerization of AA slightly reduces the electronic conductivity (Fig. S15). The measured conductivities are 0.133, 0.129, and 0.104 S m^{-1} for the pristine, crosslinked, and integrated cathodes, respectively. Given the relatively closed values, we believe that the performance disparity is primarily attributed to the different cathode–gel electrolyte interfaces. We further conducted *in situ* optical microscopy to track the evolution of the cathode–gel electrolyte interfaces upon the charge–discharge processes. The result reveals distinct gaps between the cathode and the gel interface in both the pristine and crosslinked cathodes. In contrast, the integrated cathode shows no obvious interfacial gap, confirming the robustness of the integrated structure during cycling (Fig. S16). The versatility of this integrated configuration was further verified in Zn||α-MnO_2 batteries (see the structural characterization in Fig. S17). The integrated α-MnO_2 cathode exhibits superior performance compared to the pristine and crosslinked cathodes (Fig. S18), which demonstrates that our integrated design strategy is a general approach, effective beyond vanadium-based cathodes.

The kinetics of the integrated cathode is further revealed by GITT (galvanostatic intermittent titration technique) analysis (Fig. 3a and S19). The diffusion coefficient of the pristine cathode gradually increases within the first few hours, indicating the "activation process". In contrast, we did not observe such a phenomenon on the integrated cathode. In addition, the Zn^{2+} diffusion coefficient is one order of magnitude higher than that of the pristine cathode. These results suggest that seamlessly connected cathode–electrolyte interfaces could facilitate ionic diffusion. *In situ* EIS analysis reveals that the impedance of the pristine cathode gradually decreases with increasing voltage but remains relatively high at lower voltages (Fig. 3b and S20). This is because poor cathode–electrolyte contact interfaces lead to high interfacial resistance and thus require high energy to overcome. Therefore, the Zn^{2+} diffusion kinetics is voltage dependent and is only promoted at higher voltages. Although the initial impedance of the integrated cathode is the highest among the three cathodes, it rapidly decreases to the lowest level upon the onset of charge–discharge cycles, reflecting fast ionic diffusion kinetics. Conversely, the impedance of the crosslinked cathode remains

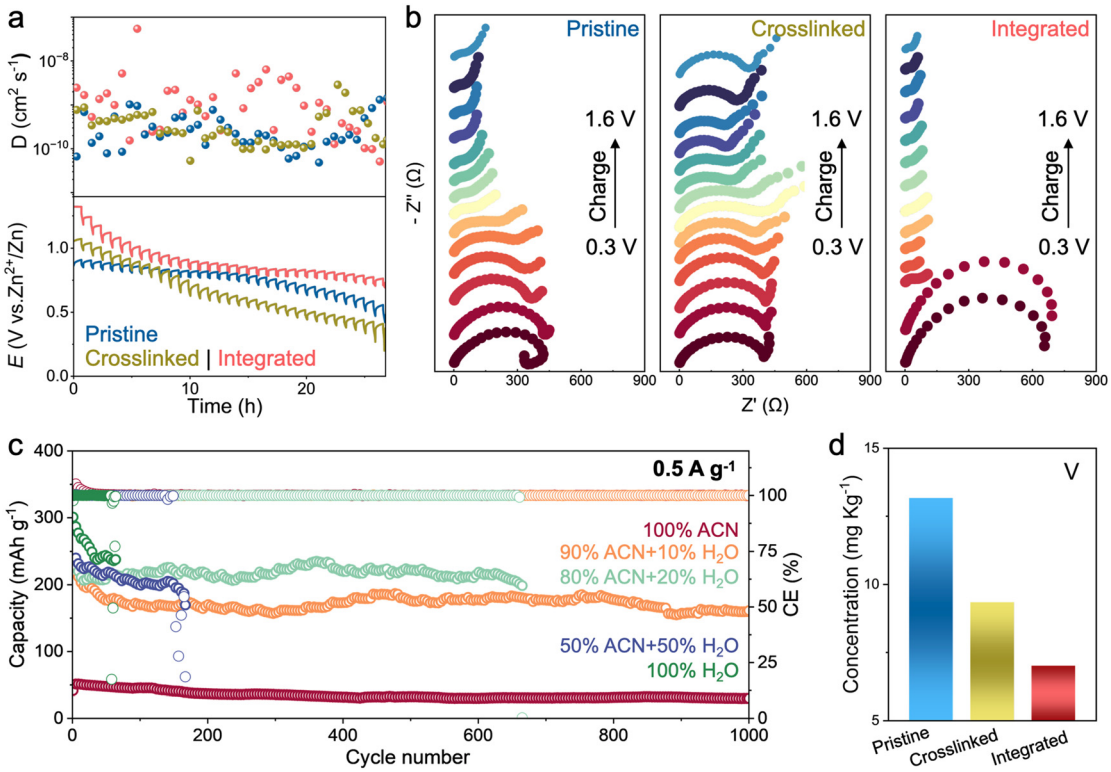

Fig. 3 Cathode–electrolyte integration exhibits superior kinetic performance. (a) The initial 25 h GITT curves of the pristine, crosslinked, and integrated cathodes. (b) *In situ* impedance spectra of pristine, crosslinked, and integrated cathodes. (c) Cycling performance at different water contents at 0.5 A g^{-1}. (d) Quantification of dissolved vanadium in the hydrogel electrolyte.

consistently within a relatively large range, suggesting limited ion diffusion kinetics.

The "activation process" is typically associated with the gradual wetting of cathode materials by aqueous electrolytes (specifically, hydrated Zn^{2+}) at the initial states. We therefore further investigated the impact of water on battery performance. We used 0.5 M $Zn(OTf)_2$ in acetonitrile (ACN) with varying H_2O contents as electrolytes (Fig. 3c). Compared to 100% ACN, the batteries using mixed electrolytes, even with only 10% H_2O, deliver significantly enhanced capacities. In addition, we observed that the battery with 100% ACN necessitates an "activation process" to achieve optimal capacity. Meanwhile, batteries with water in electrolytes do not need such a process, and higher H_2O contents generally lead to higher initial capacities. However, higher H_2O contents also result in fast capacity decay rates, due to the H_2O-promoted dissolution of vanadium species ($V_2O_5 + 3H_2O \rightarrow 2VO_2(OH)_2^- + 2H^+$). This means that the presence of water could facilitate ion diffusion and promote reaction kinetics, but sacrifices the cycling stability of the cathodes.[26] In this regard, the gel electrolytes with limited free water molecules are conducive to maintaining relatively high stability, but in turn would require an "activation process" to allow water molecules and charge carriers (*e.g.*, Zn^{2+}) to gradually diffuse from the electrolytes to the bulk surface of the cathode materials. This has been widely observed in zinc batteries with a conventional isolated cathode–gel electrolyte interface design. However, in our proposed seamlessly connected cathode–gel electrolyte interface design, the gel electrolyte and cathode active material are homogeneously mixed and integrated, significantly shortening the diffusion pathway and enhancing the kinetics, achieving full capacities without an "activation process". Moreover, the crosslinked PAM–PAA network further enhances the mechanical stability of the MVO and alleviates the dissolution of V species. The ICP-MS analysis on the gel electrolytes from the three cathodes after 100 cycles indicates that the dissolution of V and Mg in the integrated cathode is significantly suppressed (Fig. 3d and S20), which further explains the enhanced cycling performance.

A comparative analysis using finite element simulations further highlights the advantages of our proposed integrated cathode–electrolyte configuration. In conventional designs, Zn^{2+} ions slowly diffuse from the electrolyte into the bulk cathode and further interact with the active material (*i.e.*, MVO). Because of the isolated cathode and electrolyte and consequently the high interfacial resistance, this process is typically sluggish. Conversely, in the integrated cathode–electrolyte design, the cathode interior is saturated with electrolyte, enabling Zn^{2+} ions to diffuse from the surroundings to the active material smoothly and rapidly (Fig. 4a and b). Over the same duration, the concentration of Zn^{2+} ions within the cathode active material in the integrated design is higher and more uniformly distributed. This effectively shortens reaction pathways, enabling rapid ion migration and diffusion, thereby significantly accelerating the activation process during initial stages and achieving higher capacities.

In addition, during the charge and discharge processes, a significant number of Zn^{2+} ions intercalate into and de-intercalate from the active material, causing variations in the crystal structure and lattice size, as well as phase transitions between crystalline and amorphous states.[27] This results in expansion or contraction of the MVO, generating diffusion stress under

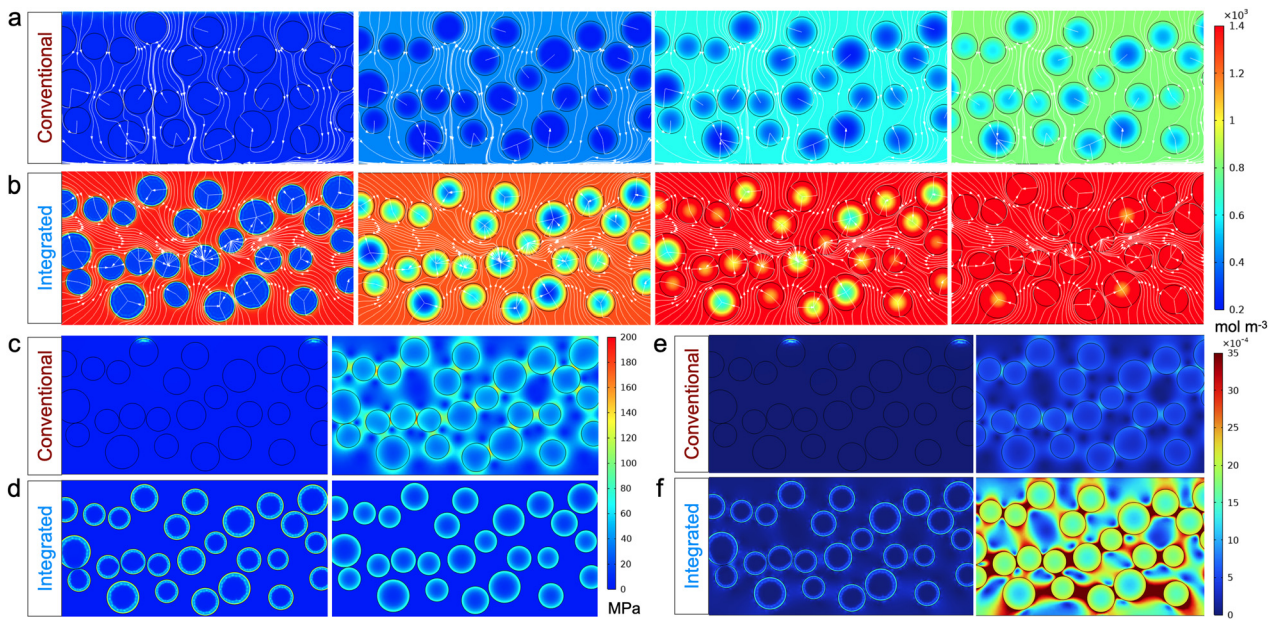

Fig. 4 Mechanical and ion diffusion simulation as a demonstration for the difference between the cathode–electrolyte integrated design and the conventional design. Simulated distributions of Zn^{2+} concentration for (a) the conventional design and (b) the integrated design. Von Mises stress for (c) the conventional design and (d) the integrated design. Equivalent strain for (e) the conventional design and (f) the integrated design.

the constraints of adjacent particles, current collectors, and external packaging. The diffusion of Zn^{2+} ions within the active material would also create a concentration gradient, leading to uneven Zn^{2+} concentrations at different locations, which further induces inhomogeneous deformation and corresponding diffusion stress.[28] Mises stress distribution simulation analysis on the cathode active material (Fig. 4c and d) reveals that at the same Zn^{2+} concentration, the integrated cathode–electrolyte design exhibits superior mechanical constraint effects. The stress distribution is more uniform and smaller, which is conducive to maintaining excellent structural stability. Conversely, in conventional designs, the cathode active materials experience higher stresses, particularly in localized areas, indicating a higher risk of structural damage and further performance deterioration.

Furthermore, during charge and discharge processes, continuous electrochemical reactions and material deformation occur within the battery, leading to ongoing changes in the shape of the cathode based on its usage state.[29] Over time, significant alterations in the structure and stability of the cathode can impact the battery's performance. We then conducted strain analysis on the cathode (Fig. 4e and f). The gel electrolyte within the integrated cathode–electrolyte configuration exhibits excellent flexibility, providing a buffering effect.[30] Consequently, this integrated design can withstand greater deformation without failure within the same timeframe, demonstrating better mechanical properties and significantly improving cycling stability. In contrast, conventional designs demonstrate inadequate mechanical performance, rendering the cathode vulnerable to expansion during the charge and discharge processes. This susceptibility can result in structural damage, negatively impacting the lifespan of the battery. It is important to note that in real-world scenarios, the actual contact conditions and non-spherical nature of cathode active material particles may generate more localized stress hotspots, potentially leading to more severe mechanical failures.

Conclusions

We propose a seamlessly connected cathode–gel electrolyte interface design by integrating the cathode and gel electrolyte in aqueous zinc ion batteries. This unique integrated configuration was achieved through a new method that enables the simultaneous generation of a polymer network within the cathode and further its crosslinking with the polymer matrix of an *in situ* grown gel electrolyte. This establishes a robust cathode–gel electrolyte interface, effectively resolving interfacial contact issues and suppressing active material dissolution. Compared to conventional battery designs, where the cathode and gel electrolyte are isolated by a distinct solid–quasi-solid interface, our design significantly shortens the ion transport pathway and promotes diffusion kinetics. As a result, the Zn||MVO battery with this unique design achieved full capacity without the "activation process" that is typically needed in gel electrolyte systems. Moreover, the battery maintained a high capacity of 200 mAh g^{-1} at 0.5 A g^{-1} after 900 cycles, significantly outperforming the battery with a conventional design. The efficacy of this integrated configuration was further validated in Zn||MnO_2 batteries, demonstrating the versatility of our design. This work suggests an efficient and general strategy to enhance the electrochemical performance of battery gel electrolytes.

Author contributions

Y. Z. and H. L. conceived the project and wrote the manuscript. Y. Z., X. L., Y. W., J.-h. L. and Y. Z. conducted the material synthesis, physical characterization studies, and electrochemical tests. L. G., J.-c. L. and Z. G. performed the theoretical simulations. All co-authors contributed to the manuscript revision.

Conflicts of interest

There are no conflicts to declare.

Data availability

The datasets generated during this study are fully available within the article and the supplementary information (SI). Supplementary information is available. See DOI: https://doi.org/10.1039/d5eb00143a.

Acknowledgements

This work was supported by the Fujian Provincial Science and Technology Program for External Cooperation (2024I0001), the Natural Science Foundation of Xiamen, China (3502Z202473021), National Natural Science Foundation of China (No. 12172206), and the Fundamental Research Funds for the Central Universities, China (20720240066).

References

1 X. Yu, Z. Li, X. Wu, H. Zhang, Q. Zhao, H. Liang, H. Wang, D. Chao, F. Wang, Y. Qiao, H. Zhou and S.-G. Sun, *Joule*, 2023, **7**, 1145–1175.
2 J. Zheng, X. Liu, Y. Zheng, A. N. Gandi, X. Kuai, Z. Wang, Y. Zhu, Z. Zhuang and H. Liang, *Nano Lett.*, 2023, **23**, 6156–6163.
3 J. Zheng, Y. Wu, H. Xie, Y. Zeng, W. Liu, A. N. Gandi, Z. Qi, Z. Wang and H. Liang, *ACS Nano*, 2023, **17**, 337–345.
4 Z. Li, Z. Shu, Z. Shen, Y. Liu, Y. Ji, L. Luo, R. Li, Y. Cai, H. Ian, J. Xie and G. Hong, *Adv. Energy Mater.*, 2024, **14**, 2400572.
5 Y. Dai, C. Zhang, J. Li, X. Gao, P. Hu, C. Ye, H. He, J. Zhu, W. Zhang, R. Chen, W. Zong, F. Guo, I. P. Parkin,

D. J. L. Brett, P. R. Shearing, L. Mai and G. He, *Adv. Mater.*, 2024, **36**, 2310645.
6 H. Peng, D. Wang, F. Zhang, L. Yang, X. Jiang, K. Zhang, Z. Qian and J. Yang, *ACS Nano*, 2024, **18**, 21779–21803.
7 J. Wei, P. Zhang, J. Sun, Y. Liu, F. Li, H. Xu, R. Ye, Z. Tie, L. Sun and Z. Jin, *Chem. Soc. Rev.*, 2024, **53**, 10335–10369.
8 J. Yuan, Y. Li, Y. Ma, Y. Ruan, J. He, H. Xu, Z. Zhang, G. He and H. Chen, *Chem. – Asian J.*, 2024, **19**, e202400812.
9 X. Liu, J. Wang, P. Lv, Y. Zhang, J. Li and Q. Wei, *Energy Storage Mater.*, 2024, **69**, 103382.
10 X. Cheng, H. Wang, S. Wang, Y. Jiao, C. Sang, S. Jiang, S. He, C. Mei, X. Xu, H. Xiao and J. Han, *J. Colloid Interface Sci.*, 2024, **660**, 923–933.
11 C. Tian, J. Wang, R. Sun, T. Ali, H. Wang, B.-B. Xie, Y. Zhong and Y. Hu, *Angew. Chem., Int. Ed.*, 2023, **62**, e202310970.
12 A. Zhu, Q. Xu, J. Huang, Y. Li, F. Zhang, S. Qin, S. Li, C. Wan and H. Xie, *ACS Appl. Mater. Interfaces*, 2023, **15**, 41483–41493.
13 N. Wang, H. Liu, M. Sun, X. Ren, L. Hu, Z. Li, X. Yao, Y. Gong and C. Jia, *ACS Sustainable Chem. Eng.*, 2024, **12**, 3527–3537.
14 J. Song, M. Zhou, R. Yi, T. Xu, M. L. Gordin, D. Tang, Z. Yu, M. Regula and D. Wang, *Adv. Funct. Mater.*, 2014, **24**, 5904–5910.
15 H. Xia, G. Xu, X. Cao, C. Miao, H. Zhang, P. Chen, Y. Zhou, W. Zhang and Z. Sun, *Adv. Mater.*, 2023, **35**, e2301996.
16 S. Ji, H. Luo, S. Qin, X. Zhang, Y. Hu, W. Zhang, J. Sun, J. Xu, H. Xie, Z. Yan and K. Yang, *Adv. Energy Mater.*, 2024, **14**, 2400063.
17 Y. Qin, H. Li, C. Han, F. Mo and X. Wang, *Adv. Mater.*, 2022, **34**, 2207118.
18 L. Chen, T. Xiao, J.-L. Yang, Y. Liu, J. Xian, K. Liu, Y. Zhao, H. J. Fan and P. Yang, *Angew. Chem., Int. Ed.*, 2024, **63**, e202400230.
19 J. Zhang, R. Liu, C. Huang, C. Dong, L. Xu, L. Yuan, S. Lu, L. Wang, L. Zhang and L. Chen, *Nano Energy*, 2024, **122**, 109301.
20 P. Zhang, K. Wang, Y. Zuo, M. Wei, H. Wang, Z. Chen, N. Shang and P. Pei, *Chem. Eng. J.*, 2023, **451**, 138622.
21 M. Jiao, L. Dai, H.-R. Ren, M. Zhang, X. Xiao, B. Wang, J. Yang, B. Liu, G. Zhou and H.-M. Cheng, *Angew. Chem.*, 2023, **135**, e202301114.
22 H. Li, J. Sun, S. Qin, Y. Song, Z. Liu, P. Yang, S. Li, C. Liu and C. Shen, *Adv. Funct. Mater.*, 2023, **33**, 2301773.
23 R. Epping, U. Panne, W. Hiller, T. Gruendling, B. Staal, C. Lang, A. Lamprou and J. Falkenhagen, *Anal. Sci. Adv.*, 2020, **1**, 34–45.
24 J. G. H. Hermens, A. Jensma and B. L. Feringa, *Angew. Chem., Int. Ed.*, 2022, **61**, e202112618.
25 J. Guan, L. Shao, L. Yu, S. Wang, X. Shi, J. Cai and Z. Sun, *Chem. Eng. J.*, 2022, **443**, 136502.
26 F. Ming, Y. Zhu, G. Huang, A.-H. Emwas, H. Liang, Y. Cui and H. N. Alshareef, *J. Am. Chem. Soc.*, 2022, **144**, 7160–7170.
27 J. Dai, S. Tan, L. Wang, F. Ling, F. Duan, M. Ma, Y. Shao, X. Rui, Y. Yao, E. Hu, X. Wu, C. Li and Y. Yu, *ACS Nano*, 2023, **17**, 20949–20961.
28 L. Ji and Z. Guo, *Acta Mech. Sin.*, 2018, **34**, 187–198.
29 J. Wang, X. Li, J. Yang, W. Sun, Q. Ban, L. Gai, Y. Gong, Z. Xu and L. Liu, *ChemSusChem*, 2021, **14**, 2056–2066.
30 T. Dam, S. S. Jena and A. Ghosh, *J. Appl. Phys.*, 2019, **126**, 27214–27223.